

# Variable Eddington Factor Acceleration of Lumped Linear Discontinuous Galerkin/Mixed Finite Element Source Iteration

Samuel S. Olivier, Jim E. Morel

Department of Nuclear Engineering  
Texas A&M University  
College Station, TX 77843

## Abstract

*Insert abstract here*

## Keywords

Source Iteration acceleration, Lumped Linear Discontinuous Galerkin, Mixed Finite Element Method

## Running Head

Variable Eddington Factor Method

## Corresponding Author

Jim E. Morel, Phone: (979)845-6072, FAX: (979)845-6075, E-mail: *morel@tamu.edu*.

# 1 Introduction

The Variable Eddington Factor (VEF) method, also known as Quasi-Diffusion (QD), was one of the first nonlinear methods for accelerating source iterations in  $S_N$  calculations [1]. It is comparable in effectiveness to both linear and nonlinear forms of Diffusion-Synthetic Acceleration (DSA), but it offers much more flexibility than the DSA. Stability can only be guaranteed with DSA if the diffusion equation is differenced in a manner consistent with that of the  $S_N$  equations [2]. Modern  $S_N$  codes often use advanced discretization schemes such as discontinuous Galerkin (DG) since classic discretization schemes such as step and diamond are not suitable for radiative transfer calculations in the High Energy Density Laboratory Physics (HEDLP) regime or coupled electron-photon calculations. Diffusion discretizations consistent with the DG  $S_N$  discretizations cannot actually be expressed in diffusion form, but rather must be expressed in first-order or  $P_1$  form, and are much more difficult to solve than standard diffusion discretizations [3]. Considerable effort has gone into the development of “partially consistent” diffusion discretizations that yield a stable DSA algorithm with some degree of degraded effectiveness, but such discretizations are also generally difficult to develop [4, 5, 6]. A great advantage of the VEF method is that the drift-diffusion equation that accelerates the  $S_N$  source iterations can be discretized in any valid manner without concern for consistency with the  $S_N$  discretization. When the VEF drift-diffusion equation is discretized in a way that is “non-consistent,” the  $S_N$  and VEF drift-diffusion solutions for the scalar flux do not necessarily become identical when the iterative process converges. However, they do become identical in the limit as the spatial mesh is refined, and the difference between the two solutions is proportional to the spatial truncation errors associated with the  $S_N$  and drift-diffusion discretizations. In general the order accuracy of the  $S_N$  and VEF drift-diffusion solutions will be the lowest order accuracy

of their respective independent discretizations. Although the  $S_N$  solution obtained with such a “non-consistent” VEF method is not conservative, the VEF drift-diffusion solution is in fact conservative. This is particularly useful in multiphysics calculations where the low-order VEF equation can be coupled to the other physics components rather than the high-order  $S_N$  equations. Another advantage of the non-consistent approach is that even if the  $S_N$  spatial discretization scheme does not preserve the thick diffusion limit [7], that limit will generally be preserved using the VEF method.

The purpose of this paper is to investigate the application of the VEF method with the 1-D  $S_N$  equations discretized with the lumped linear-discontinuous method (LLDG) and the drift-diffusion equation discretized using the constant-linear mixed finite-element method (MFEM). To our knowledge, this combination has not been previously investigated. Our motivation for this investigation is that MFEM methods are now being used for high-order hydrodynamics calculations [8]. A radiation transport method compatible with MFEM methods is clearly desirable for developing a MFEM radiation-hydrodynamics code. Such a code would combine thermal radiation transport with hydrodynamics. However, MFEM methods are inappropriate for the standard first-order form of the transport equation. Thus the use of the VEF method with a DG  $S_N$  discretization and a MFEM drift-diffusion discretization suggests itself. Here we define a VEF method that should exhibit second-order accuracy since both the transport and drift-diffusion discretizations are second-order accurate in isolation. In addition, our VEF method should preserve the thick diffusion limit, which is essential for radiative transfer calculations in the HEDLP regime. We use the lumped rather than the standard Linear Discontinuous Galerkin discretization because lumping yields a much more robust scheme, and robustness is essential for radiative transfer calculations in the HEDLP regime. Because this is an initial study, we simplify the investigation by consid-

ering only the one-group neutron transport equation rather than the full radiative transfer equations, which include a material temperature equation as well as the radiation transport equation. The vast majority of relevant properties of a VEF method for radiative transfer can be tested with an analogous method for one-group neutron transport. Furthermore, a high-order DG-MFEM VEF method could be of interest for neutronics in addition to radiative transfer calculations. A full investigation for radiative transfer calculations will be carried out in a future study.

The remainder of this paper is organized as follows. First, we describe the VEF method analytically. Then we describe our discretized  $S_N$  equations, followed by a description of the discretized VEF drift-diffusion equation. We next give computational results. More specifically, we describe two ways to represent the  $S_N$  variable Eddington factor in the MHEM drift-diffusion equation and several ways to construct the  $S_N$  scattering source from the drift-diffusion solution for the scalar flux. Each of these options yields a different VEF method. The accuracy of these methods is then compared to that of the standard LLDG  $S_N$  solution for several test problems, and the iterative convergence rate of these methods is compared to that of the LLDG  $S_N$  equations with fully-consistent  $S_2$ SA acceleration. Finally, we give conclusions and recommendations for future work.

## 2 The VEF Method

### 2.1 The Algorithm

Here, we describe the VEF method for a planar geometry, fixed-source problem:

$$\mu \frac{\partial \psi}{\partial x}(x, \mu) + \sigma_t(x) \psi(x, \mu) = \frac{\sigma_s(x)}{2} \int_{-1}^1 \psi(x, \mu') d\mu' + \frac{Q(x)}{2}, \quad (1)$$

where  $\mu = \cos \theta$  is the cosine of the angle of flight  $\theta$  relative to the  $x$ -axis,  $\sigma_t(x)$  and  $\sigma_s(x)$  the total and scattering macroscopic cross sections,  $Q(x)$  the isotropic fixed-source and  $\psi(x, \mu)$  the angular flux. Applying the Discrete Ordinates ( $S_N$ ) angular discretization yields the following set of  $N$  coupled, ordinary differential equations:

$$\mu_n \frac{d\psi_n}{dx}(x) + \sigma_t(x)\psi_n(x) = \frac{\sigma_s(x)}{2}\phi(x) + \frac{Q(x)}{2}, 1 \leq n \leq N, \quad (2)$$

where  $\psi_n(x) = \psi(x, \mu_n)$  is the angular flux in direction  $\mu_n$ . The  $\mu_n$  are stipulated by an  $N$ -point Gauss quadrature rule such that the scalar flux,  $\phi(x)$ , can be numerically integrated with:

$$\phi(x) = \sum_{n=1}^N w_n \psi_n(x), \quad (3)$$

where the  $w_n$  are the quadrature weights corresponding to the  $\mu_n$ .

The VEF method decouples Eq. 2 by lagging the scattering term:

$$\mu_n \frac{d\psi_n^{\ell+1/2}}{dx}(x) + \sigma_t(x)\psi_n^{\ell+1/2}(x) = \frac{\sigma_s(x)}{2}\phi^\ell(x) + \frac{Q(x)}{2}, 1 \leq n \leq N, \quad (4)$$

where the superscripts indicate the iteration index. The scalar flux used in the scattering term,  $\phi^\ell$ , is assumed to be known either from the previous iteration or from the initial guess if  $\ell = 0$ . In Source Iteration (SI), the update

$$\phi(x)^{\ell+1} = \phi(x)^{\ell+1/2} \quad (5)$$

is used. However, this is slow to converge in optically thick and highly scattering systems. Instead, the VEF method solves the VEF drift diffusion equations found by taking the first

two angular moments of Eq. 2:

$$\frac{d}{dx} J^{\ell+1}(x) + \sigma_a(x) \phi^{\ell+1}(x) = Q(x), \quad (6a)$$

$$\frac{d}{dx} \langle \mu^2 \rangle^{\ell+1/2}(x) \phi^{\ell+1}(x) + \sigma_t(x) J^{\ell+1}(x) = 0, \quad (6b)$$

where  $J^{\ell+1}(x)$  is the current and

$$\langle \mu^2 \rangle^{\ell+1/2}(x) = \frac{\int_{-1}^1 \mu^2 \psi^{\ell+1/2}(x, \mu) d\mu}{\int_{-1}^1 \psi^{\ell+1/2}(x, \mu) d\mu} \xrightarrow{S_N} \frac{\sum_{n=1}^N \mu_n^2 \psi_n^{\ell+1/2}(x) w_n}{\sum_{n=1}^N \psi_n^{\ell+1/2}(x) w_n} \quad (7)$$

the Eddington factor. The scattering term in Eq. 4 is then updated with the VEF drift diffusion scalar flux found by solving Eqs. 6a and 6b. This process of solving Eq. 4 for the  $\psi_n(x)$ , computing the Eddington factor, solving the VEF drift diffusion equation for the scalar flux, and updating the scattering term with the VEF drift diffusion scalar flux is repeated until convergence.

Acceleration occurs because the angular shape of the angular flux, and thus the Eddington factor, converges much faster than the scalar flux. In addition, the VEF equations model the contributions of all scattering events at once, reducing the dependence on source iterations to introduce scattering information.

In addition to acceleration, this scheme allows the  $S_N$  equations and drift diffusion equations to be solved with arbitrarily different spatial discretization methods. The following sections present the application of the Lumped Linear Discontinuous Galerkin (LLDG) spatial discretization to the  $S_N$  equations and the Mixed Finite Element Method (MFEM) to the VEF drift diffusion equations.

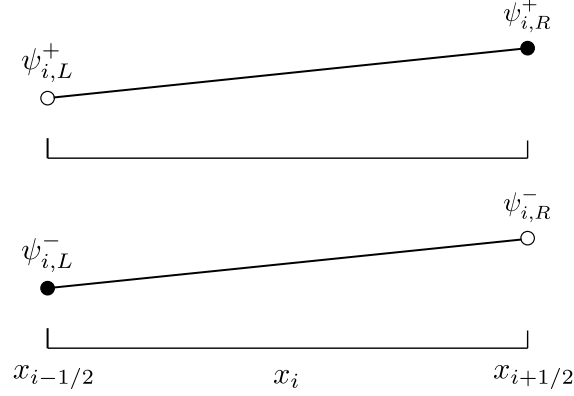


Figure 1: The distribution of unknowns in an LLDG cell. The superscript  $+$  and  $-$  indicate the angular fluxes for  $\mu_n > 0$  and  $\mu_n < 0$ , respectively.

## 2.2 Lumped Linear Discontinuous Galerkin $S_N$

The spatial grid and distribution of unknowns for an LLDG cell are shown in Fig. 1. The cell centers are integral and the cell edges are half integral. The two unknowns in each cell for each discrete angle are the left and right edge discontinuous angular fluxes,  $\psi_{n,i,L}^{\ell+1/2}$  and  $\psi_{n,i,R}^{\ell+1/2}$ .

The LLDG discretization of Eq. 4 is then:

$$\mu_n \left( \psi_{n,i}^{\ell+1/2} - \psi_{n,i-1/2}^{\ell+1/2} \right) + \frac{\sigma_{t,i} h_i}{2} \psi_{n,i,L}^{\ell+1/2} = \frac{\sigma_{s,i} h_i}{4} \phi_{i,L}^{\ell} + \frac{h_i}{4} Q_{i,L}, \quad (8a)$$

$$\mu_n \left( \psi_{n,i+1/2}^{\ell+1/2} - \psi_{n,i}^{\ell+1/2} \right) + \frac{\sigma_{t,i} h_i}{2} \psi_{n,i,R}^{\ell+1/2} = \frac{\sigma_{s,i} h_i}{4} \phi_{i,R}^{\ell} + \frac{h_i}{4} Q_{i,R}, \quad (8b)$$

where  $h_i$ ,  $\sigma_{t,i}$ , and  $\sigma_{s,i}$  are the cell width, total cross section, and scattering cross section in cell  $i$ . The discontinuous scalar fluxes,  $\phi_{i,L/R}^{\ell}$ , are assumed to be known from the previous iteration or the initial guess when  $\ell = 0$ . The cell edged angular fluxes are uniquely defined

by upwinding:

$$\psi_{n,i-1/2}^{\ell+1/2} = \begin{cases} \psi_{n,i-1,R}^{\ell+1/2}, & \mu_n > 0 \\ \psi_{n,i,L}^{\ell+1/2}, & \mu_n < 0 \end{cases}, \quad (9a)$$

$$\psi_{n,i+1/2}^{\ell+1/2} = \begin{cases} \psi_{n,i,R}^{\ell+1/2}, & \mu_n > 0 \\ \psi_{n,i+1,L}^{\ell+1/2}, & \mu_n < 0 \end{cases}. \quad (9b)$$

The cell centered angular flux is the average of the left and right discontinuous edge fluxes:

$$\psi_{n,i}^{\ell+1/2} = \frac{1}{2} \left( \psi_{n,i,L}^{\ell+1/2} + \psi_{n,i,R}^{\ell+1/2} \right). \quad (10)$$

Equations 8a, 8b, 9a, 9b, and 10 can be combined and rewritten as

$$\begin{bmatrix} \mu_n + \sigma_{t,i} h_i & \mu_n \\ -\mu_n & \sigma_{t,i} + \mu_n \end{bmatrix} \begin{bmatrix} \psi_{n,i,L}^{\ell+1/2} \\ \psi_{n,i,R}^{\ell+1/2} \end{bmatrix} = \begin{bmatrix} \frac{\sigma_{s,i} h_i}{2} \phi_{i,L}^{\ell} + \frac{h_i}{2} Q_{i,L} + 2\mu_n \psi_{n,i-1,R}^{\ell+1/2} \\ \frac{\sigma_{s,i} h_i}{2} \phi_{i,R}^{\ell} + \frac{h_i}{2} Q_{i,R} \end{bmatrix}, \quad (11)$$

for sweeping from left to right ( $\mu_n > 0$ ) and

$$\begin{bmatrix} -\mu_n + \sigma_{t,i} h_i & \mu_n \\ -\mu_n & -\mu_n + \sigma_{t,i} h_i \end{bmatrix} \begin{bmatrix} \psi_{n,i,L}^{\ell+1/2} \\ \psi_{n,i,R}^{\ell+1/2} \end{bmatrix} = \begin{bmatrix} \frac{\sigma_{s,i} h_i}{2} \phi_{i,L}^{\ell} + \frac{h_i}{2} Q_{i,L} \\ \frac{\sigma_{s,i} h_i}{2} \phi_{i,R}^{\ell} + \frac{h_i}{2} Q_{i,R} - 2\mu_n \psi_{n,i+1,L}^{\ell+1/2} \end{bmatrix}, \quad (12)$$

for sweeping from right to left ( $\mu_n < 0$ ). The right hand sides of Eqs. 11 and 12 are known as the scalar flux from the previous iteration, the fixed source, and the angular flux entering from the previous cell are all known. By supplying the flux entering the left side of the first cell, the positive-angled solution can be propagated from left to right by solving Eq. 11. Similarly, supplying the incident flux on the right boundary allows the negative-angled solution to be propagated from right to left with Eq. 12.



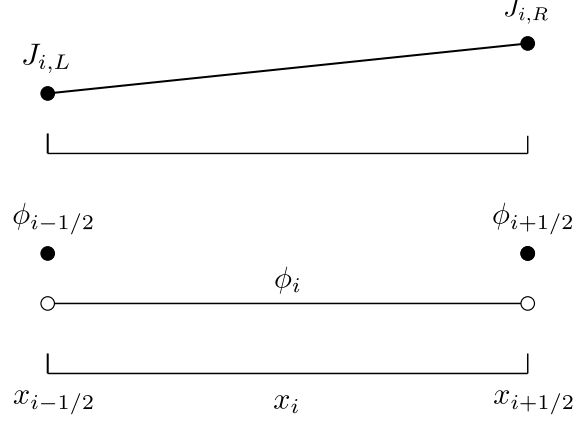


Figure 2: The distribution of unknowns in cell  $i$  for MFEM.

### 2.3 Mixed Finite Element Method VEF Drift Diffusion

The unknowns in an MFEM cell are depicted in Fig. 2. The scalar flux is constant within the cell with discontinuous jumps at the cell edges and the current is a linear function defined by:

$$J_i(x) = J_{i,L}B_{i,L}(x) + J_{i,R}B_{i,R}(x), \quad (13)$$

where  $J_{i,L/R}$  are the currents at the left and right edges of the cell and

$$B_{i,L}(x) = \begin{cases} \frac{x_{i+1/2}-x}{h_i}, & x \in [x_{i-1/2}, x_{i+1/2}] \\ 0, & \text{otherwise} \end{cases}, \quad (14a)$$

$$B_{i,R}(x) = \begin{cases} \frac{x-x_{i-1/2}}{h_i}, & x \in [x_{i-1/2}, x_{i+1/2}] \\ 0, & \text{otherwise} \end{cases}, \quad (14b)$$

are the MFEM basis functions. The spatial grid used in this step is identical to the grid used in the LLDG  $S_N$  step.

The MFEM representation yields five unknowns per cell:  $\phi_{i-1/2}$ ,  $\phi_i$ ,  $\phi_{i+1/2}$ ,  $J_{i,L}$ , and  $J_{i,R}$ . An equation for  $\phi_i$  is found by integrating Eq. 6a over cell  $i$ :

$$J_{i,R} - J_{i,L} + \sigma_{a,i} h_i \phi_i = Q_i h_i, \quad (15)$$

where  $\sigma_{a,i}$  and  $Q_i$  are the absorption cross section and source in cell  $i$ . Equations for  $J_{i,L/R}$  are found by multiplying Eq. 6b by  $B_{i,L/R}$  and integrating over cell  $i$ :

$$-\langle \mu^2 \rangle_{i-1/2} \phi_{i-1/2} + \langle \mu^2 \rangle_i \phi_i + \sigma_{t,i} h_i \left( \frac{1}{3} J_{i,L} + \frac{1}{6} J_{i,R} \right) = 0, \quad (16a)$$

$$\langle \mu^2 \rangle_{i+1/2} \phi_{i+1/2} - \langle \mu^2 \rangle_i \phi_i + \sigma_{t,i} h_i \left( \frac{1}{6} J_{i,L} + \frac{1}{3} J_{i,R} \right) = 0, \quad (16b)$$

where the fixed source has been assumed to be isotropic. The Eddington factors,  $\langle \mu^2 \rangle_{i(\pm 1/2)}$ , are computed using the angular fluxes from the LLDG  $S_N$  step according to:

$$\langle \mu^2 \rangle_{i(\pm 1/2)} = \frac{\sum_{n=1}^N \mu_n^2 \psi_{n,i(\pm 1/2)} w_n}{\sum_{n=1}^N \psi_{n,i(\pm 1/2)} w_n}, \quad (17)$$

where the cell edge angular fluxes are defined by Eq. 9a and 9b and the cell centered angular flux by Eq. 10. Eliminating  $J_{i,R}$  from Eq. 16a and  $J_{i,L}$  from Eq. 16b yields:

$$J_{i,L} = \frac{-2}{\sigma_{t,i} h_i} \left\{ 2 [\langle \mu^2 \rangle_i \phi_i - \langle \mu^2 \rangle_{i-1/2} \phi_{i-1/2}] - [\langle \mu^2 \rangle_{i+1/2} \phi_{i+1/2} - \langle \mu^2 \rangle_i \phi_i] \right\}, \quad (18a)$$

$$J_{i,R} = \frac{-2}{\sigma_{t,i} h_i} \left\{ 2 [\langle \mu^2 \rangle_{i+1/2} \phi_{i+1/2} - \langle \mu^2 \rangle_i \phi_i] - [\langle \mu^2 \rangle_i \phi_i - \langle \mu^2 \rangle_{i-1/2} \phi_{i-1/2}] \right\}. \quad (18b)$$

A fourth equation is found by enforcing continuity of current:

$$J_{i,R} = J_{i+1,L} . \quad (19)$$

Using the definitions of  $J_{i,L}$  and  $J_{i,R}$  from Eqs. 18a and 18b in the balance equation (Eq. 15) and continuity equation (Eq. 19) reduces the system to three unknowns per cell:  $\phi_{i-1/2}$ ,  $\phi_i$ , and  $\phi_{i+1/2}$ . The resulting balance and continuity equations are:

$$-\frac{6}{\sigma_{t,i}h_i}\langle\mu^2\rangle_{i-1/2}\phi_{i-1/2} + \left(\frac{12}{\sigma_{t,i}h_i}\langle\mu^2\rangle_i + \sigma_{a,i}h_i\right)\phi_i - \frac{6}{\sigma_{t,i}h_i}\langle\mu^2\rangle_{i+1/2}\phi_{i+1/2} = Q_i h_i , \quad (20a)$$

$$\begin{aligned} -\frac{2}{\sigma_{t,i}h_i}\langle\mu^2\rangle_{i-1/2}\phi_{i-1/2} + \frac{6}{\sigma_{t,i}h_i}\langle\mu^2\rangle_i\phi_i - 4\left(\frac{1}{\sigma_{t,i}h_i} + \frac{1}{\sigma_{t,i+1}h_{i+1}}\right)\langle\mu^2\rangle_{i+1/2}\phi_{i+1/2} \\ + \frac{6}{\sigma_{t,i+1}h_{i+1}}\langle\mu^2\rangle_{i+1}\phi_{i+1} - \frac{2}{\sigma_{t,i+1}h_{i+1}}\langle\mu^2\rangle_{i+3/2}\phi_{i+3/2} = 0 . \end{aligned} \quad (20b)$$

On the interior,  $\phi_{i-1/2} = \phi_{(i-1)+1/2}$ . Thus, Eqs. 20a and 20b are sufficient to specify the center and edge scalar fluxes on the interior. The remaining unknowns,  $\phi_{1/2}$  and  $\phi_{I+1/2}$ , are set by the boundary conditions. Equations for  $\phi_{1/2}$  and  $\phi_{I+1/2}$  are found by setting the equations for  $J_{1,L}$  and  $J_{I,R}$  to a supplied boundary current. For example, a vacuum condition can be applied on the left boundary through a modified Marshak boundary:

$$J_{1,L} = B_{1/2}\phi_{1/2} , \quad (21)$$

where  $J_{1,L}$  is defined in Eq. 18a and

$$B_{1/2} = \frac{\sum_{n=1}^N |\mu_n| \psi_{n,1/2} w_n}{\sum_{n=1}^N \psi_{n,1/2} w_n} . \quad (22)$$

A left reflecting condition is set by

$$J_{1,L} = 0. \quad (23)$$

This system of  $2I + 1$  equations can be assembled into a matrix of both cell centered and cell edge scalar fluxes and solved with a banded matrix solver of bandwidth five.

Increased consistency Two methods have been tested for generating the cell centered Eddington factors: averaging the cell edge values and representing the LLDG angular flux as a linear function of the MFEM basis functions:

$$\langle \mu^2 \rangle_i(x) = \frac{\sum_{n=1}^N \mu_n^2 [\psi_{n,i,L} B_{i,L}(x) + \psi_{n,i,R} B_{i,R}(x)]}{B_{i,L}(x) \sum_{n=1}^N w_n \psi_{n,i,L} + B_{i,R}(x) \sum_{n=1}^N w_n \psi_{n,i,R}}. \quad (24)$$

Equation 24 is a rational polynomial and cannot be integrated analytically. In this case, two point Gauss quadrature was used to numerically integrate Eq. 24 over the interior of cell  $i$ :

$$\langle \mu^2 \rangle_i = \frac{1}{2} [\langle \mu^2 \rangle_i(x_{i,L}) + \langle \mu^2 \rangle_i(x_{i,R})], \quad (25)$$

where

$$x_{i,L/R} = \frac{h_i}{2} \mp \frac{x_{i+1/2} + x_{i-1/2}}{2\sqrt{3}} \quad (26)$$

are the quadrature points in the cell.

Once the MFEM scalar flux has been found, the LLDG scattering term must be reconstructed. Two methods have been tested: no reconstruction and van Leer limited cell centered slope reconstruction. The no reconstruction method sets the LLDG discontinuous left and right scalar flux to the MFEM edge scalar flux:

$$\phi_{i,L/R} = \phi_{i\mp 1/2}, \quad (27)$$

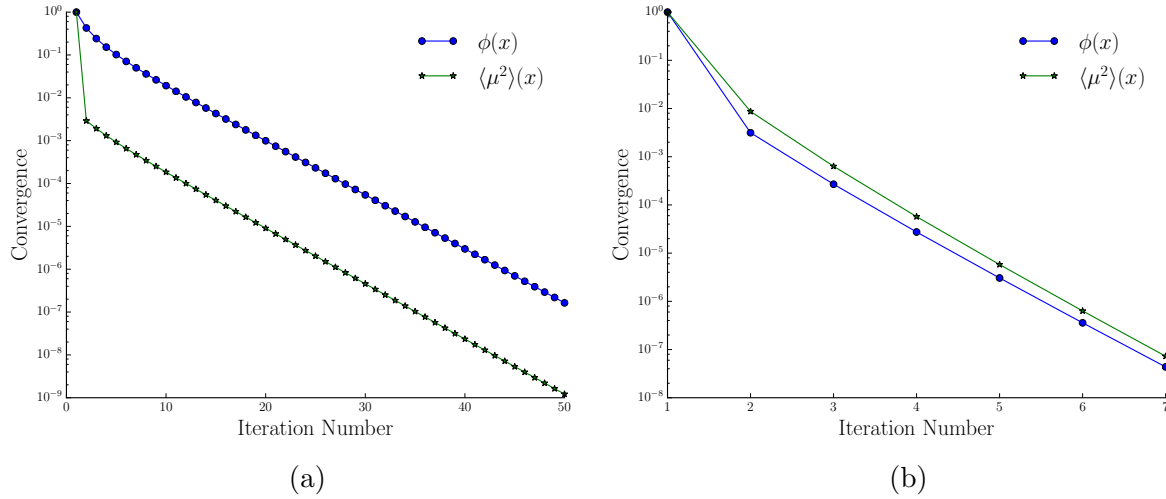


Figure 3: The convergence rate for  $\phi(x)$  and  $\langle \mu^2 \rangle(x)$  for (a) unaccelerated and (b) VEF accelerated SI.

where the left hand side is the reconstructed LLDG flux used in the scattering term of Eq. 4 and the right hand side the MFEM drift diffusion flux. The van Leer cell centered reconstruction is:

$$\phi_{i,L/R} = \phi_i \mp \frac{1}{4} \xi_{\text{van Leer}} [(\phi_{i+1} - \phi_i) + (\phi_i - \phi_{i-1})], \quad (28)$$

where  $\xi_{\text{van Leer}}$  the slope limiter given in [9].

### 3 Computational Results

Figure 3a shows the iterative convergence as a function of unaccelerated iteration number for the scalar flux and the Eddington factor. The Eddington factor's large drop in relative norm between the first and second iterations supports the claim that the angular shape of the angular flux, and thus the Eddington factor, converges rapidly. When compared to Fig.

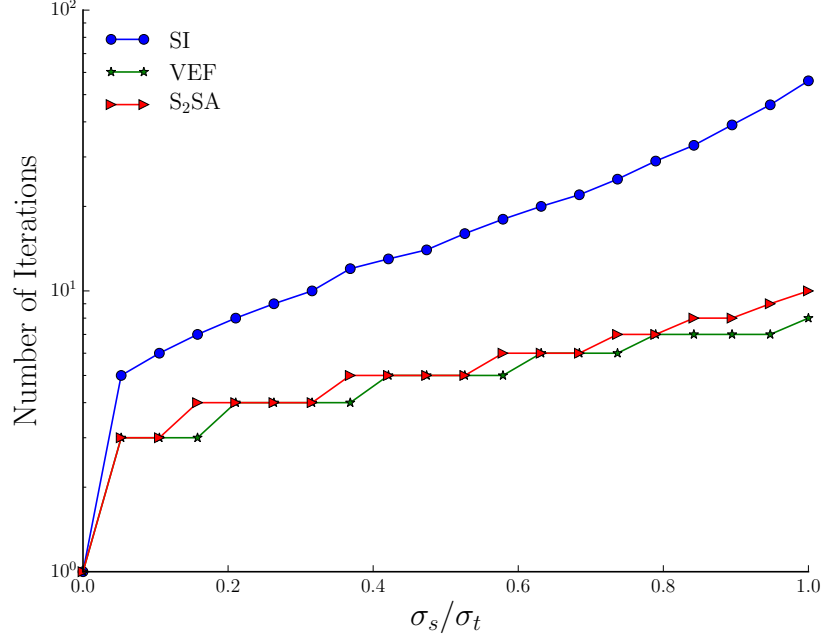


Figure 4: A comparison of the number of iterations required for Source Iteration, VEF acceleration, and S<sub>2</sub>SA to converge for varying ratios of  $\sigma_s$  to  $\sigma_t$ .

3b, a plot of the iterative convergence for the VEF method, it is clear that the VEF method transfers the fast rate of convergence of the Eddington factor to the scalar flux.

To compare SI, VEF, and consistently differenced S<sub>2</sub>SA, a test problem with a reflecting left boundary and a vacuum right boundary was used. This system was discretized into 50 spatial cells.  $\sigma_t$  was set to  $1 \text{ cm}^{-1}$  leading to an optical thickness per cell of 0.2. The convergence tolerance was set to  $10^{-6}$ . Figure 4 shows the number of iterations required for convergence for SI, VEF, and S<sub>2</sub>SA for varying ratios of  $\sigma_s$  to  $\sigma_t$ . Aside from  $\sigma_s/\sigma_t = 0$  where acceleration is not possible, the ratio of unaccelerated to VEF accelerated iterations ranged from 1.6 to 7. This suggests that acceleration is occurring and that the VEF method is not just doing twice the amount of work per iteration. In addition, the VEF method performed similarly to S<sub>2</sub>SA.

Reconstruction Method	Eddington Representation	Order	$C$	$R^2$
None	Average	1.997	0.682	$9.9999 \times 10^{-1}$
None	Rational Polynomial	1.998	0.687	1.0000
Center	Average	2.007	0.726	$9.9992 \times 10^{-1}$
Center	Rational Polynomial	2.009	0.732	$9.9991 \times 10^{-1}$

Table 1: The order of accuracy, error, and  $R^2$  values for the permutations of the two Eddington representation methods and two slope reconstruction methods.

The Method of Manufactured Solutions (MMS) was used to compare the accuracy of the VEF method as the cell width was decreased. The L2 norm of the difference between the numerical and MMS solutions was compared at five logarithmically spaced cell widths between 0.5 mm and 0.01 mm. A line of best fit of the form

$$E = Ch^n \quad (29)$$

was used to find the order of accuracy,  $n$ , and the constant of proportionality,  $C$ , of the numerical error,  $E$ . These values are provided in Table 1 for the permutations of the two reconstruction methods and two angular flux representation methods. All of the permutations are second order accurate and have similar overall accuracy. This suggests that slope reconstruction and Eddington representation do not affect numerical accuracy.

The convergence between unaccelerated SI and the VEF method was compared as a function of cell width for a simple homogeneous slab and for Reed’s problem. In both cases, the left boundary was reflecting and the right boundary was vacuum. The homogeneous slab had a scattering ratio of 0.75. The cross sections and source for Reed’s problem are provided in Table 2. The L2 norm of the difference between the SI solution and VEF solution is plotted for the four permutations of no reconstruction, van Leer slope limited reconstruction, average Eddington representation, and rational polynomial Eddington representation in Figures 5a

	Region 1	Region 2	Region 3	Region 4	Region 5
$q$	10	0	0	0	1
$\Sigma_t$	10	0.001	1	5	1
$\Sigma_a$	10	0	0.1	0	0.1
Domain	$0 \leq x < 2$	$2 \leq x < 4$	$4 \leq x < 6$	$6 \leq x < 7$	$7 \leq x \leq 8$

Table 2: The cross sections and source used for Reed’s problem.

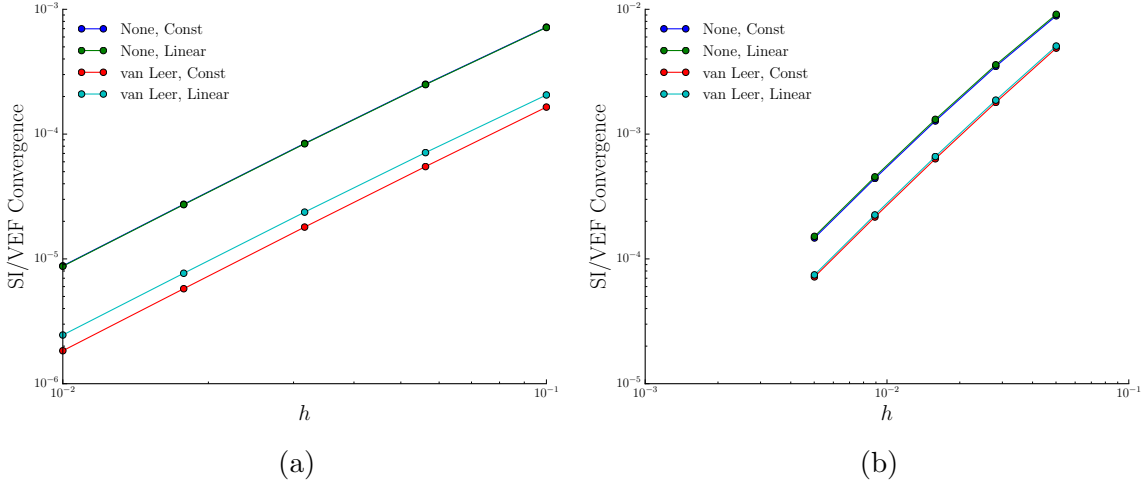


Figure 5: The L2 norm of the difference between SI and the four permutations of the VEF method as the cell spacing is decreased for (a) the homogeneous slab problem and (b) Reed’s problem.

and 5b for the homogeneous slab problem and Reed’s problem.

In the homogeneous problem, VEF with van Leer limited slope reconstruction was five times more convergent than VEF without reconstruction. Use of the rational polynomial Eddington representation decreased the van Leer reconstruction convergence by 30%.

Lastly, slope reconstruction and Eddington representation were tested in the diffusion limit. The cross sections and source were scaled according to:

$$\sigma_t(x) \rightarrow \sigma_t(x)/\epsilon, \quad (30a)$$



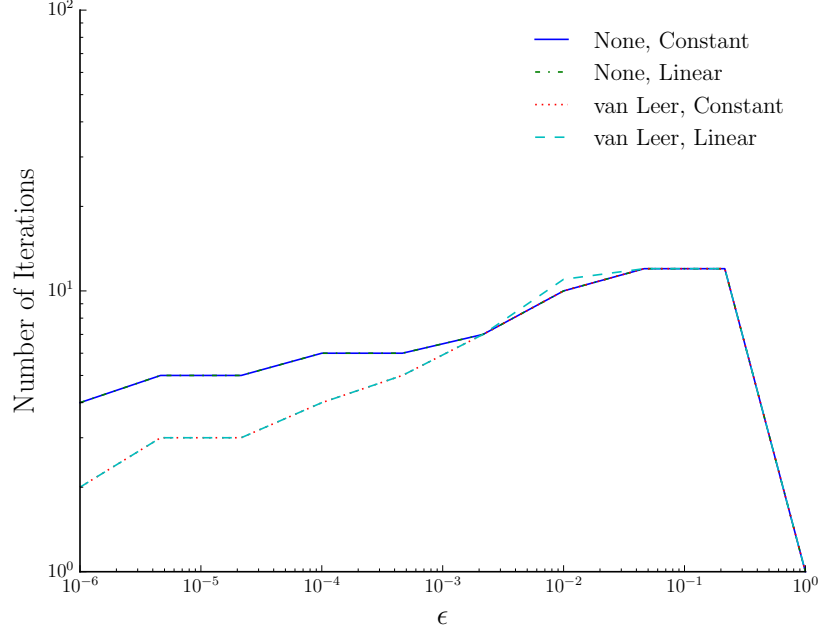


Figure 6: The number of iterations required for convergence for the permutations of slope reconstruction and angular flux representation in the diffusion limit.

$$\sigma_s(x) \rightarrow \epsilon \sigma_s(x), \quad (30b)$$

$$Q(x) \rightarrow \epsilon Q(x). \quad (30c)$$

As  $\epsilon \rightarrow 0$ , the system becomes diffusive. The number of iterations for convergence within a tolerance of  $10^{-8}$  as  $\epsilon \rightarrow 0$  is plotted in Fig. 6. The error between the VEF solution and the exact diffusion solution is provided in Fig. 7. This supports the claim that the VEF method is robust as all four permutations survived the diffusion limit.

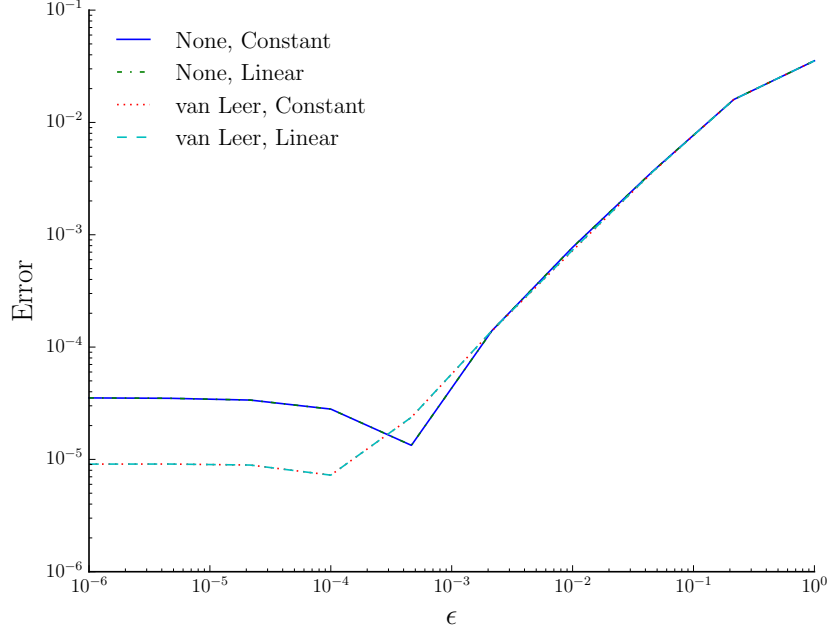


Figure 7: The error between the VEF methods and the exact diffusion solution as  $\epsilon \rightarrow 0$ .

## 4 Conclusions and Future Work

We have presented the VEF method for one-group neutron transport in slab geometry and the pairing of LLDG for the  $S_N$  transport step and MFEM for the drift diffusion acceleration step. We have numerically demonstrated that the LLDG/MFEM VEF method accelerates Source Iteration by transferring the rapid convergence of the angular shape of the angular flux to the scalar flux. The VEF method performed similarly to consistently differenced  $S_2SA$ .

Methods for increased consistency between LLDG and MFEM were also presented. This included a cell centered slope reconstruction method that will be needed for radiative transfer calculations. It was shown that the inconsistent, partially consistent, and fully consistent methods were second-order accurate as expected from the orders of accuracy of LLDG and

MFEM in isolation and that all of the VEF methods were robust in the diffusion limit. In addition, while this nonlinear scheme produces two solutions, one from  $S_N$  and one from drift diffusion, the solutions were shown to converge as the mesh was refined for both homogeneous and inhomogeneous systems.

Future work includes extending the VEF method presented in this paper to the radiative transfer equations and verifying the VEF method in 2 and 3 dimensional systems.

## References

- [1] M.L. Adams and E.W. Larsen. Fast iterative methods for discrete-ordinates particle transport calculations. *Progress in Nuclear Energy*, 40(1):3–159, 2002.
- [2] R.E. Alcouffe. Diffusion synthetic acceleration methods for the diamond-differenced discrete-ordinates equations. *Nuclear Science and Engineering*, 64:344–355, 1977.
- [3] J.S. Warsa, T.A. Wareing, and J.E. Morel. Fully-consistent diffusion-synthetic acceleration of linear discontinuous  $s_n$  transport discretizations on unstructured tetrahedral meshes. *Nuclear Science and Engineering*, 141:235–251, 2002.
- [4] J.E. Morel and E.W. Larsen. A multiple balance approach for differencing the  $s_n$  equations. *Nuclear Science and Engineering*, 105:1–15, 1990.
- [5] Marvin L. Adams and William R. Martin. Diffusion synthetic acceleration of discontinuous finite element transport iterations. *Nuclear Science and Engineering*, 111:145–167, 1992.

- [6] Yaqi Wang and Jean C. Ragusa. Diffusion synthetic acceleration for high-order discontinuous finite element  $s_n$  transport schemes and application to locally refined unstructured meshes. *Nuclear Science and Engineering*, 166(2):145–166, 2010.
- [7] Edward W. Larsen, J.E. Morel, and Warren F. Miller, Jr. Asymptotic solutions of numerical transport problems in optically thick, diffusive regimes. *Journal of Computational Physics*, 69:283–324, 1987.
- [8] V. Dobrev, Tz. Kolev, and R. Rieben. High-order curvilinear finite element methods for lagrangian hydrodynamics. *SIAM Journal on Scientific Computing*, 34:B606–B641, 2012.
- [9] B. van Leer. Towards the ultimate conservative difference scheme I: The quest for monotonicity. *Lecture Notes in Physics*, 18:163–168, 1973.